

## Graphene nanohybrids for enhanced catalytic activity and large surface area

**Sabeen Fatima**, Department of Physics, School of Natural Sciences (SNS), National University of Science & Technology (NUST), Islamabad 44000, Pakistan

**S. Irfan Ali**, Shenzhen Key Laboratory of Advanced Thin Films and Applications, College of Physics and Energy, Shenzhen University, Shenzhen 518060, China

**Daniyal Younas**, Department of Physics, School of Natural Sciences (SNS), National University of Science & Technology (NUST), Islamabad 44000, Pakistan

**Amjad Islam**, College of Materials Engineering, Fujian Agriculture and Forestry University, Fuzhou-350002, China

**Deji Akinwande**, Microelectronics Research Center, University of Texas at Austin, Texas 78758, USA

**Syed Rizwan**, Department of Physics, School of Natural Sciences (SNS), National University of Science & Technology (NUST), Islamabad 44000, Pakistan

Address all correspondence to Syed Rizwan at [syedrizwanh83@gmail.com](mailto:syedrizwanh83@gmail.com)

(Received 31 May 2018; accepted 5 September 2018)

### Abstract

Nanohybrids containing graphene and bismuth ferrite have been actively employed as efficient photo-catalysts these days owing to the low rate of charge carrier's ( $e^- - h^+$ ) recombination, moderate surface area with a suitable range of band-gaps. We have synthesized nanohybrids of graphene oxide (GO) and doped  $\text{BiFeO}_3$  using a co-precipitation method and the doping elements were lanthanum and manganese, hence called BLFMO/GO nanohybrids. The surface area of BLFMO [La = 15% increased from  $6.8 \text{ m}^2/\text{g}$  (for pure) to  $62.68 \text{ m}^2/\text{g}$  (in nanohybrid)]. Also, the bandgap of the BLFMO/GO nanohybrid reduced significantly up to 1.75 eV. The resulting BLFMO/GO nanohybrid represents significantly higher catalytic activity (96% in 30 min) than the pure  $\text{BiFeO}_3$  (30% in 30 min).

### Introduction

Ferrites belong to a large class of metal oxides and have been a center of extensive study because of the simultaneous presence of electrical with magnetic properties inside the same material. Due to the low cost, shape versatility, wide frequency range (10–50 kHz), temperature and time stability, high resistivity, economical assembly, and large selection material, ferrites have an edge over other magnetic materials.<sup>[1]</sup> At the nanoscale, ferrites show unique properties which are very much distinct from their identical parts present inside bulk. The change in properties of ferrite nanoparticles is due to significant structural changes, joint rearrangements of electrons because of the reduced dimensionality and the surface atoms dominance.<sup>[2–4]</sup> In all these years, enough work has been done over ferrite nanoparticles with quite attractive industrial and scientific applications like rotary transformers, telecommunication, magnetic memory cores, magnetic recording heads, and electrical appliances.<sup>[5]</sup>

Multiferroics are scientifically as well as technologically fascinating materials because of the cross coupling between their ferroic order states within a single material. Bismuth ferrite ( $\text{BiFeO}_3$ ), abbreviated as BFO, perhaps is an alone perovskite structure depicting not even strong ferroelectric but magnetic effect naturally at a normal room temperature.<sup>[6]</sup> The perovskite frameworks are of vast importance in today's

research field due to exhibiting magnetic effect, excellent multi-ferroic properties, and photocatalytic behavior. These characteristics are beneficial to various applications including nonvolatile memory devices,<sup>[7]</sup> photoelectrochemical solar cells,<sup>[8]</sup> capacitors having magneto-capacitive effects,<sup>[9]</sup> and nonlinear optics.<sup>[10]</sup> For enhancing the electromagnetic behavior and structural properties of BFO, the researchers have doped it with numerous elements. This improvement in various physical properties exhibits an opportunity for the implementation of co-doped BFO nanostructures in our industry and different medical fields.

Carbon, an abundantly found element in nature, is a significant element among others in its family. Graphene is a two-dimensional allotropic form of carbon comprised of a single atomic layer organized in the shape of a hexagon. Graphene being the thinnest material can easily cover approximately  $0.052 \text{ nm}^2$  area and also  $0.77 \text{ mg}/\text{m}^2$  denser.<sup>[11]</sup> In comparison with the steel, graphene is hundred times mechanically stronger but much lighter in weight.<sup>[12]</sup> In recent years, the graphene charm has covered the whole industry and owing to its exceptional optical behavior,<sup>[13]</sup> mechanical strength, and electromagnetic properties,<sup>[14]</sup> it is treated as a most valuable material not even for the electronic industry but also for optical media. Its potential uses are limitless ranging from unique kinds of malleable electronics which on one hand can be

worn over clothes but can be folded easily to put into a pocket, hence resulting a complete fresh generation consisting of small flexible computers, highly productive solar cells, and ultra-fast smart phones. Chemically, multilayer graphene is prepared by peeling of flake graphite with a suitable oxidizing and reducing agents since the single sheet of graphene is unstable and is challenging to fabricate under normal conditions. Graphene nano-hybrids are the simplest structures which can be easily prepared with the addition of a small amount of graphene into polymers or different kinds of metals.<sup>[15]</sup> Graphene presence inside these nano-hybrids not even makes them mechanically much stronger and conductive but also more heat resistive in comparison with their pure forms. The hybrid structures of graphene with different magnetic materials or ferrites play a vital role in many applications such as band-gap tuning, various types of sensors, dye-sorption, antimicrobial activity, oil spill pollution, photocatalysis, etc.<sup>[16]</sup>

Photocatalysts, comprised of semiconductors, have been widely used for the removal of pollutants from air and water over last few decades.<sup>[17–19]</sup> A good photocatalyst should have minimal electron–hole (charge carriers produced when light falls) recombination, promote efficient charge transfer, and should absorb a wide solar spectrum. Under these specifications, different oxides<sup>[20,21]</sup> and their composites<sup>[22–24]</sup> have been reported for degrading the organic molecules under irradiation of ultraviolet (UV) light. TiO<sub>2</sub> has been very important in the photocatalytic activity as it was the first discovered UV light driven photocatalytic material.<sup>[25]</sup> In TiO<sub>2</sub>, photo-generated electrons and holes recombine at a fast rate which in turn makes it an inefficient photocatalyst.<sup>[26,27]</sup> Since, sunlight is accessible as an easy and sufficient cheap source of electromagnetic radiation whose major portion is comprised of visible light, the finest way of its usage is purification of water and for doing so we need to design a photocatalyst which can actively perform its duty under irradiation of solar light. Freshly, it has been explored that BFO is not even an important multiferroic magnetoelectric material but also stimulates effectively under solar light. BFO nanoparticles exhibit a significant photocatalytic activity due to highly stable crystal structure, a sufficient band-gap, and vast surface area.<sup>[28]</sup> By fabricating smaller particles with large surfaces it is possible to break down the organic pollutants in a shorter time duration. The water degradation occurs due to the oxidation of organic molecules which results in carbon dioxide (CO<sub>2</sub>) and water (H<sub>2</sub>O); both are harmless to the living tissues. The effective separation within holes and electrons acts as a vital entity in the process of oxidation and also in photo-catalytic activity. If a photocatalyst fails to maintain a sufficient electron–hole separation then the charge carriers with in the photocatalyst will recombine and hence there will be no oxidation. Graphene hybrids with BFO provides an active way of increasing photocatalytic behavior by maintaining a sufficient separation within the photo-generated electron–hole pairs.<sup>[29,30]</sup> Single crystalline perovskite BFO nanocubes were synthesized by a simple microwave method for good photocatalytic applications.<sup>[31]</sup>

Under UV-vis irradiation, BFO nanoplatelets and nanosheets showed enhanced photocatalytic behavior in degrading methyl orange (MO).<sup>[32]</sup> A multi-band semiconductor Bi<sub>2</sub>Fe<sub>4</sub>O<sub>9</sub> was used for improving photocatalysis by promoting the electron–hole separation.<sup>[33]</sup> Ferrite bismuth photocatalysts were fabricated via ultrasound and efficiently removed the methylene blue and rhodamine B under sunlight.<sup>[34,35]</sup> Gd-doped BFO nanoparticles were reported as good photocatalysts with a low recombination rate of photo-generated charge carriers.<sup>[36]</sup> Mesoporous gyroid-like La- and Mn-doped BFO nanostructures having a surface area of 9 m<sup>2</sup>/g were reported as effective photocatalysts.<sup>[37]</sup> A more efficient photocatalytic system for degrading different organic dyes like methylene blue also known as methylthioninium chloride, Congo red (CR), and methylene violet have been recently developed by doping of Gd and Sn with BFO.<sup>[38]</sup> Doping of rare earths by a sol–gel method showed an enhanced effect in photocatalytic activity of BFO.<sup>[39]</sup> In the BFO–graphene composite, graphene behaves as an electron acceptor and can easily capture the electrons and hence, more holes are available for photocatalysis. Another important point is that the graphene bears a comparatively bigger surface area (calculated approximately 2600 m<sup>2</sup>/g for single layer<sup>[40]</sup>) and is expected to increase the surface area with an external material used to make the composite material. Hence, a desire for exploring advances in graphene-based nano-hybrids with tunable band-gap and enhanced surface area is always a challenging field for researchers. Graphene–semiconductor-based systems were discussed as attractive photocatalysts in both environmental and energy applications.<sup>[41]</sup> A successful degradation process of MO with BiFeO<sub>3</sub>–graphene nanocomposite was reported with an irradiation time of 5 h.<sup>[42]</sup> BiFeO<sub>3</sub>–graphene nano-hybrids were prepared through a hydrothermal process with an increased surface area ranging from 4.1 to 37 m<sup>2</sup>/g and reported as good photocatalysts.<sup>[30]</sup> A Bi<sub>25</sub>FeO<sub>40</sub>–graphene nanocomposite was used as an efficient photocatalyst with an increase of surface area up to 59.0 m<sup>2</sup>/g.<sup>[43]</sup> Bi<sub>2</sub>Fe<sub>4</sub>O<sub>9</sub>/rGO were used to degrade hydrophobic pollutants in a competent way.<sup>[44,45]</sup> Photodegradation of BPA was completed in 70 min using BFO/rGO nanocomposites.<sup>[46]</sup>

In the current work, we address the fabrication of functionalized graphene oxide (GO) using a chemical method. The nano-hybrids of ferrite nanoparticles and GO were successfully synthesized by a co-precipitation (co-ppt) method and their enhanced photocatalytic activity is reported.

## Experimental section

BFO nanoparticles, doped with 8% lanthanum (La), also called as BLFO, co-doped with manganese (Mn = 5%, 10%, 15%, 20%, and 25%) nanoparticles, abbreviated, respectively, as BLFO, BLFMO-5, BLFMO-10, BLFMO-15, BLFMO-20, and BLFMO-25, were synthesized with the help of the sol-gel method. A detailed fabrication scheme can be found elsewhere.<sup>[38]</sup>

### Preparation of GO

3 g of graphite powder was mixed with nitric acid ( $\text{HNO}_3$ ) and 98% concentrated sulfuric acid ( $\text{H}_2\text{SO}_4$ ) in a ratio of 1:2. The stirring of mixture was done for 40 min. Then,  $\text{KMnO}_4$  was gradually added into the acidic mixture under an ice bath and stirred for 60 min by maintaining the temperature below 8 °C and the color of the mixture was then turned dark green from black. After adding potassium permanganate carefully, the temperature was raised to 38 °C for 30 min. Then, 200 mL deionized (DI) water was poured into this mixture at a slow rate for 60 min and the temperature was then increased to 98 °C, resulting in the change of color of mixture to dark brown. Maintaining the same temperature, the DI water and 30 mL of 35% concentrated  $\text{H}_2\text{O}_2$  was added and the mixture color was completely turned bright yellow. The solution was filtered and washed four to five times with 200 mL of 1 M hydrochloric acid (HCl) solution and DI water for neutralizing the pH of the mixture. Graphite oxide was exfoliated ultrasonically for 2 h and this solution was subjected to centrifugation at 12,000 rpm for 40 min; the GO was collected in the form of a paste. The paste was desiccated under 60 °C for approximately 24 h.

### Preparation of nanohybrids

The dispersion of 1 mg/mL of GO was prepared in DI water. The 0.02 molar dispersions of BLFO and BLFMOs were made in acetic acid and ethylene glycol in a 1:1 ratio through sonication under 60 °C for 150 min. Both dispersions were mixed together and sonicated for 15 min. Then, the mixture was placed on a magnetic stirrer and stirring was done for 60 min at 85 °C. The nanohybrid was turned into a precipitate and was seen clearly separated from the rest of the solution. After stirring, the mixture was then set aside to cool down at normal room temperature. After cooling the precipitates were washed using DI water several times followed by vacuum filtration. A paste-like filtrate was obtained after filtration and was then dried in an oven for 24 h at 50 °C. The as obtained thin paper-like dried form was further crushed to obtain a fine powder. The structural analysis and surface morphology were studied using x-ray diffraction (XRD) with a monochromatic radiation of  $\lambda = 1.54 \text{ \AA}$ , scanning electron microscopy, (SEM) and transmission electron microscopy (TEM), respectively. X-ray photon spectroscopy (XPS) was used to check the chemical bonding among the BLFMO nanoparticles and GO inside BLFMO/GO nanohybrids. Photo-luminescence (PL) emission measurements were also performed for checking the charge carrier (electron–hole) recombination rate inside nanohybrids. Brunauer Emmett Teller (BET) measurement was done for calculating the material's surface area by the nitrogen adsorption–desorption isotherm and the photocatalytic degradation was performed to analyze the enhanced efficiency of the nanohybrids as compared with the pure ferrite nanoparticles.

The diffuse reflectance spectra (DRS) and photocatalytic properties of BLFMO/GO samples were measured by UV-vis

DRS using a UV-vis spectrophotometer (Hitachi U3310). A 300 W xenon lamp was acted as a visible-light source. A 15 cm distance was maintained between the strip lamp and fluid level. The 0.1 g of the photocatalyst and 0.1 L of aqueous solution of dye (initial concentration = 0.1 mg/mL) were involved inside the response system. The aqueous suspension was stirred for 2 h in the dark to verify that the suspension had attained an adsorption evenness. The 3 mL of the blend was extracted from the suspension after every 30 min during the photoreaction process. The photocatalyst was removed from this blend using a centrifuge and the residual clear liquid was further subjected to UV-vis spectroscopy.

## Results and discussion

### Structure and morphology

The crystal structure of GO, BLFO, and BLFMO nanoparticles, BLFO/GO and BLFMO/GO nanohybrids are verified by XRD given in Fig. 1. The XRD patterns of GO are shown in Fig. 1(a). It is obvious from the figure that one major peak appears at an angle of 11.2° for the (001) plane due to oxidation of graphite with an interlayer spacing of 7.8 Å and the second peak appears at an angle of 42.3° showing the disordered graphitic (101) plane with a *d*-spacing of 2.1 Å. Generally, the *d*-spacing among the materials is proportional to the extent of oxidation. So, the increase in the interlayer distance from 3.4 Å (for graphite) to 7.8 Å results in successful oxidation and hence, incorporation of oxygen functional groups inside the graphite layers with few structural defects.

Figure 1(b) shows the XRD analysis patterns of BLFO and BLFMO nanoparticles with the changing Mn concentration. All peaks correspond to the conventional *hkl* planes of (012), (104), (110), (006), (202), (024), (116), (112), (018), and (214) in comparison with the XRD standard JCPDS card: 20-0169. With the inclusion of La inside BFO nanoparticles results in a distortion in the rhombohedral perovskite crystal structure which is why the intensity of some peaks is decreased, as is already discussed.<sup>[47]</sup> A low impurity phase also appears in the BLFO compound which is suppressed in BLFMO by compensating the bismuth/iron vacancies upon Mn substitution. By moving from BLFO to BLFMO, the overlapping of the peaks shows a complete phase change of the rhombohedral crystal structure to the orthorhombic crystal structure due to addition of Mn concentration.<sup>[37]</sup> The increase in Mn concentration till 15% creates an increment of peak position toward higher angle with a decrease in lattice constant because the interplanar spacing is inversely proportional to the angle. This decrease in *d*-spacing is due to the replacement of larger ionic radii, i.e., Fe atoms with smaller ionic radii element, i.e., Mn. After 15% of Mn concentration, the peaks shift again toward small angle because of the compressive strain within the crystal lattice. Widening inside the peaks for BLFMO-20 and BLFMO-25 is owing to the creation of defect states and trapping of Mn atoms. The trapping produces strain inside the lattice and hence, decreases the crystallite size.<sup>[48]</sup> The calculated particle sizes for BLFMO,

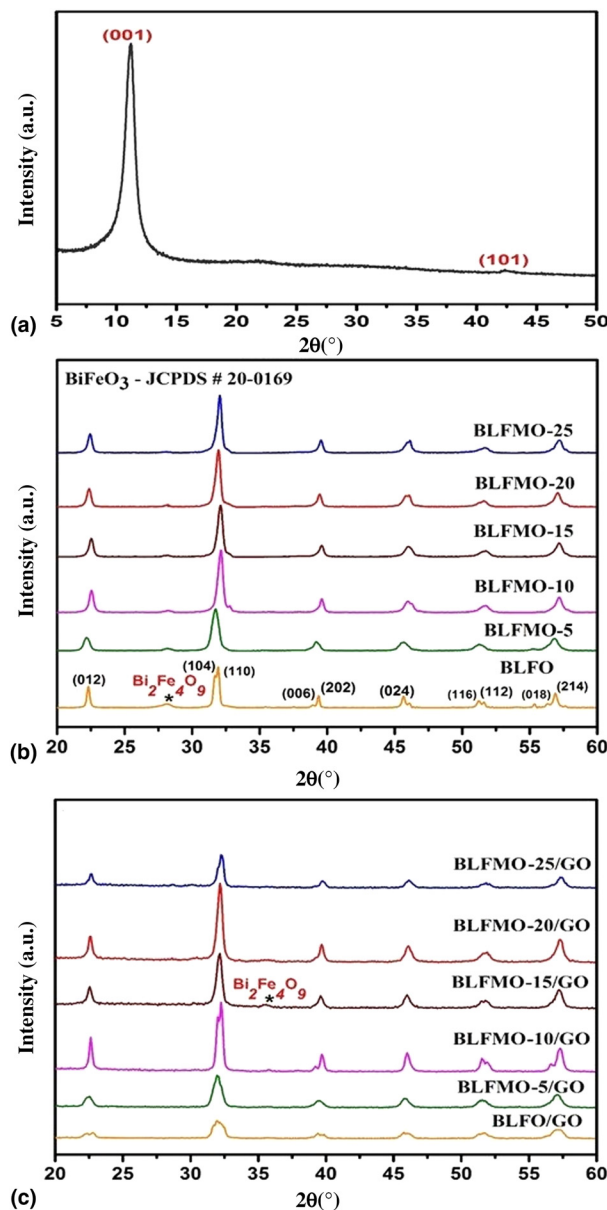


**Figure 1.** The XRD patterns of (a) GO, (b) BLFO, BLFMO (5%, 10%, 15%, 20%, and 25% Mn) nanoparticles, and (c) BLFO/GO, BLFMO/GO nanohybrids with Mn concentration ranging from 5% to 25%.

BLFMO-5, BLFMO-10, BLFMO-15, BLFMO-20, and BLFMO-25 are 24.1, 16.3, 19, 19.5, 20.2, and 20.3 nm.

The XRD peaks of BLFO/GO and BLFMO/GO hybrids are shown in Fig. 1(c). No extra peak is observed in the XRD pattern except a bismuth iron oxide impurity peak at 32.4° (in correspondence with the standard JCPDS card: 20-0836). The disappearance of GO peak in nanohybrids is due to the damage of GO structure upon the crystal growth of BLFO or BLFMO. The temperature and ultra-sonication also helps in removing oxygen functional groups and hence, non-appearance of the GO peak in the hybrid structure. This results in formation of

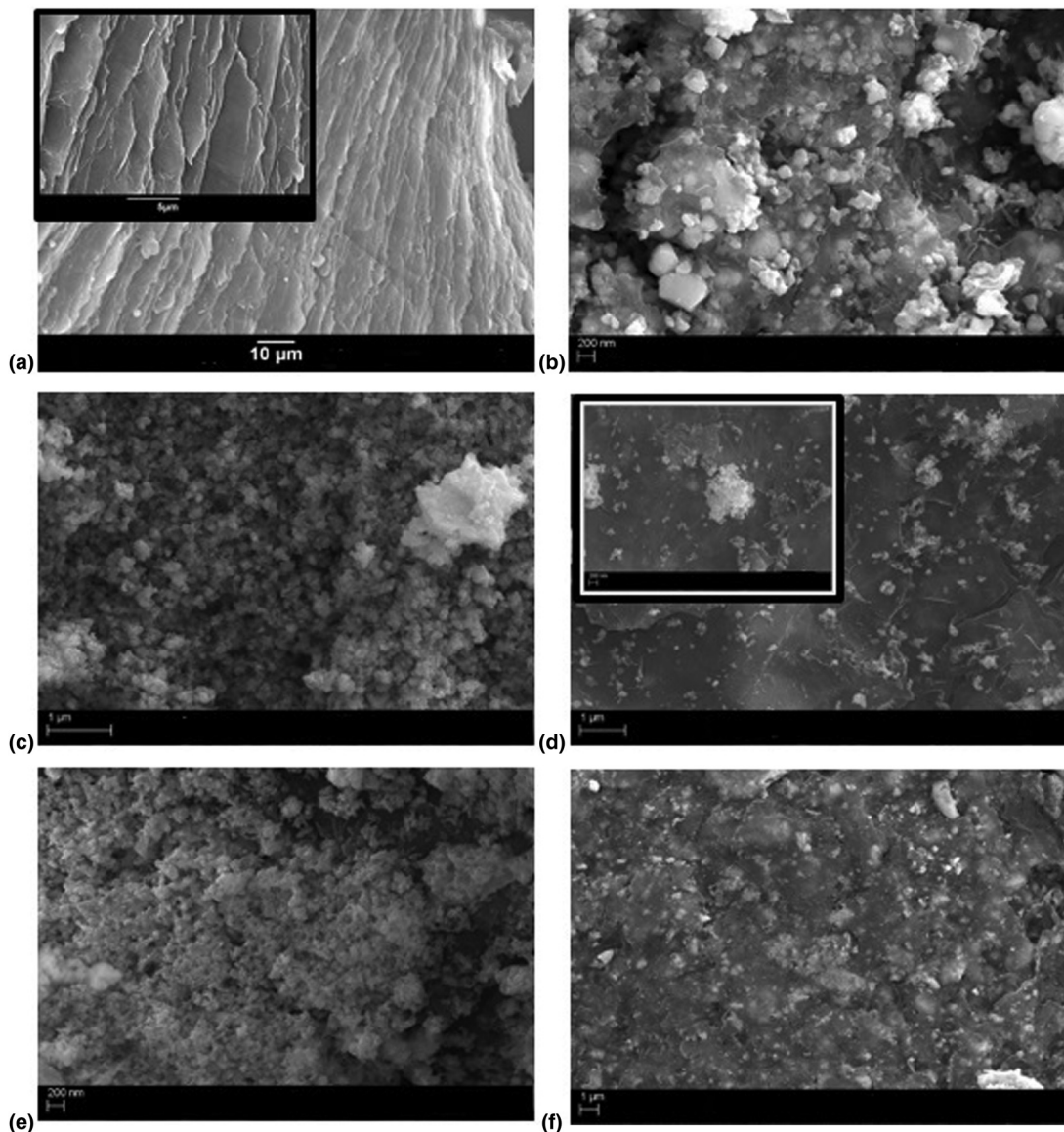
more sp<sup>2</sup> domains in graphene sheets.<sup>[46]</sup> The peaks' intensity is decreased which shows that the crystallization of BFLO and BFLMO is also affected by incorporation of graphene into the perovskite crystal structure. Hence, the hybrid crystals will have a low degree of periodicity. In addition, the hybrid peaks are also broadened due to small crystallite size as compared with the pure BLFO and BLFMO nanoparticles. The increased melding of graphene sheets inside the nucleation centers causes the delay of the crystallization process and helps in formation of uniform nanohybrid.<sup>[49]</sup> In BLFMO-10/GO, splitting of (104) and (110) is due to the presence of less amount of graphene inside the nanohybrid hence, the periodicity is high. The particle size calculated using Scherrer's formula for BLFO/GO is 12 nm, while for BLFMO-5/GO, BLFMO-10/GO, BLFMO-20/GO, and BLFMO-25/GO is 14, 23, 19.3, 19.9, and 20 nm.

Figure 2 shows the SEM images showing the surface morphology of GO sheets, BLFO, BLFMO-5/GO, BLFMO-15/GO, BFLMO-20/GO, and BFLMO-25/GO nanohybrids.

The layered structure of GO is shown in Fig. 2(a). GO sheets are stacked together and can be seen clearly in the inset image of SEM. The hybrid contains a mixed morphology of both, GO sheets and mesoporous BLFO nanoparticles [Fig. 2(b)] and BLFMO nanoparticles [Figs. 2(c)-2(f)]. In the BLFO/GO hybrid, the nanoparticles are embedded over the GO surface. In the BLFMO-5/GO composite, it is seen that the GO sheets are strongly ingrained inside the BLFO nanoparticles and the nanoparticles are completely dispersed over these nanosheets. This is the reason why it is hard to distinguish between the nanolayers and nanoparticles in these hybrid composites. In BLFMO-15/GO, well dispersed particles can be seen on the GO sheets while in the inset, intermixed particle-layer structure is formed at a scale of 200 nm. In BLFMO-20/GO, there is an agglomeration of nanoparticles due to the surface defects and in the BLFMO-25/GO hybrid, rapid growth of BLFMO nanoparticles inside the GO layers toward active sites destroy the graphene layers which is consistent with the XRD results shown.

TEM was performed to explore the structural details at higher resolution. TEM images of BLFMO-5/GO and BLFMO-15/GO are shown in Fig. 3. The thin crumpled graphene sheets are clearly visible in TEM images. The well dispersed mesoporous BLFMO nanoparticles (in spherical form) are connected at the interface with the graphene layers and also dispersed above the GO surface which indicates the successful formation of our nanohybrid. We found that the thin interconnected graphene sheets enable an increase in the surface to volume ratio and hence, increased the catalytic degradation efficiency of the nanohybrids.

XPS investigation was done in order to probe the chemical composition of BLFMO/GO nanohybrids. The XPS spectra are shown in Fig. 4. The XPS spectra give us the detailed information related to the chemical bonding present inside the BLFMO and GO. Figure 4(a) shows all chemical bonds of Bi, La, Fe, Mn, O, and C present inside the BLFMO/GO nanohybrid with respect to their binding energies.<sup>[30,50,51]</sup> The major



**Figure 2.** The FE-SEM images of (a) layered structure of graphite oxide. Inset: layers shown up to a scale of 5  $\mu\text{m}$ . (b) BLFO/GO, (c) BLFMO-5/GO, and (d) well-dispersed BLFMO nanoparticles with GO sheets in BLFMO-15/GO. Inset: nanoparticles on sheets at 200 nm. (e) BLFMO-20/GO, (f) BLFMO-25/GO showing both, nanoparticle and layer morphology mixed inside the hybrid composites.

components (Bi, C, and O) of the nanohybrid structures are also shown in Figs. 4(b)–4(d). Two main peaks of Bi4f are obtained in the range of 156–166 eV [Fig. 4(b)]. Similarly, two species are present inside C1s [Fig. 4(c)] corresponding to C@C ( $\text{sp}^2\text{C}$ ) and C–O. The signal of C–O is very much strong in the C1s electrons which is due to the incorporation of BFO over the GO surface.<sup>[30]</sup> Other species such as C–H and COOR (C@O), which are introduced onto the surface of GO during the oxidation process, have been reduced during the hybrid formation because of the introduction of BFO and thermal treatment. A major peak of O1s is centered at 532 eV as shown in Fig. 4(d). Oxygen vacancies (O KLL) are also appeared inside BFO to compensate the overall charge.<sup>[52]</sup> An impurity peak of

N1s electrons is also appeared inside the BLFMO/GO hybrid which may be introduced during oxidation of graphite and is not eliminated.

The surface area measurements of nanohybrids were obtained by the analysis of nitrogen adsorption which represents the higher surface area of BLFO/GO and BLFMOs/GO nanohybrids than the pure forms of these ferrite nanoparticles. The highest surface area of  $62.68 \text{ m}^2/\text{g}$  was observed for the BLFMO-15/GO nanohybrid. The type-IV BET isotherm and pore size distribution for BLFMO-15/GO are shown in Fig. 5. The sheet-like mesoporous system with an average pore diameter of 12.3 nm and a total pore volume of  $0.193 \text{ cm}^3/\text{g}$  with less crystallinity was observed.

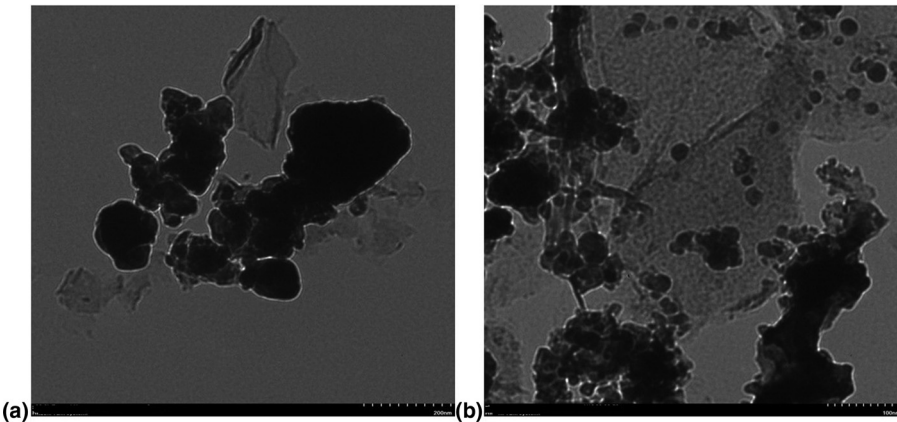


**Figure 3.** TEM images of (a) BLFMO-5/GO and (b) BLFMO-15/GO.

The addition of graphene within the nanohybrid causes the decrement inside crystallite size and hence, increment in the surface area.

The PL emission measurements were performed by using a fluorescence spectrophotometer for the BLFMO-5 and BLFMO-15 samples and the results are shown in Fig. 6. The PL spectra shown here give information regarding the photo-generated charge carrier transfer, electron–hole recombination, and migration in semiconductor photocatalysts.<sup>[53]</sup>

In the PL spectra, the much lower the peak intensity the much higher the degradation efficiency of the nanohybrid. The PL intensity for BLFO/GO and BLFMO-15/GO is higher as compared with other nanohybrids and approximately equal as the photo-degradation of dye inside both of these is 4% and 5% in 30 min. The PL intensity is lower for the BLFMO-5/GO nanohybrid whose photo-degradation efficiency is 8% in 30 min. The PL is very low in the BLFMO-25/GO nanohybrid representing the lower electron–hole recombination rate and hence higher photocatalytic activity. The dye degradation

efficiency inside BLFMO-25/GO is comparatively higher than other hybrid structures which is 15% in 30 min. Lower the PL intensity means more generation of active species (peroxides and OH<sup>-</sup> radicals) helps in enhancing the redox reactions over the hybrid surface with the organic dye molecules which results in quick and efficient dye extraction from the aqueous blend. After the introduction of graphene, the visible light generated charge carriers are effectively transported over the top of the photocatalyst under visible light irradiation as graphene behaves as a grabbing site for excited electrons and promotes an adequate charge separation over the photocatalyst surface and hence, improves the degradation efficiency of our nanohybrids.<sup>[54]</sup>

### Photocatalytic measurements

Figure 7 shows the general mechanism involved in the photo-degradation of organic molecules using BLFMO/graphene nanohybrids. The electron–hole generation under visible light

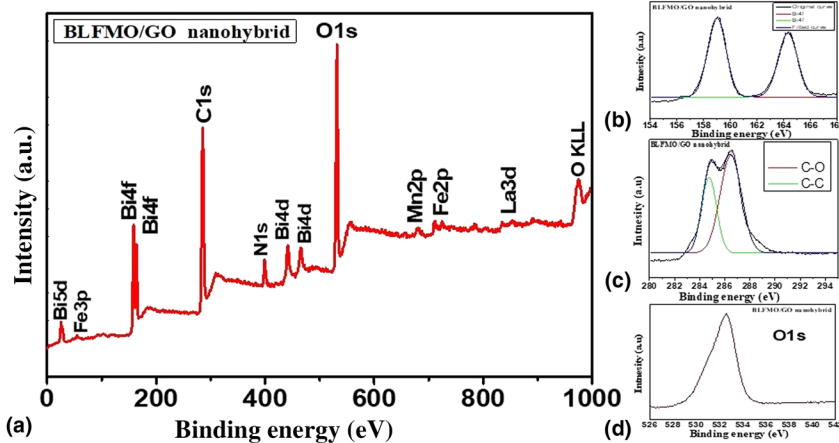


**Figure 4.** (a) XPS spectra of the BLFMO-15/GO nanohybrid. (b) XPS spectra for Bi4f. (c) XPS spectra for C1s containing C<sub>60</sub>C and C–O. (d) XPS spectra for O1s.

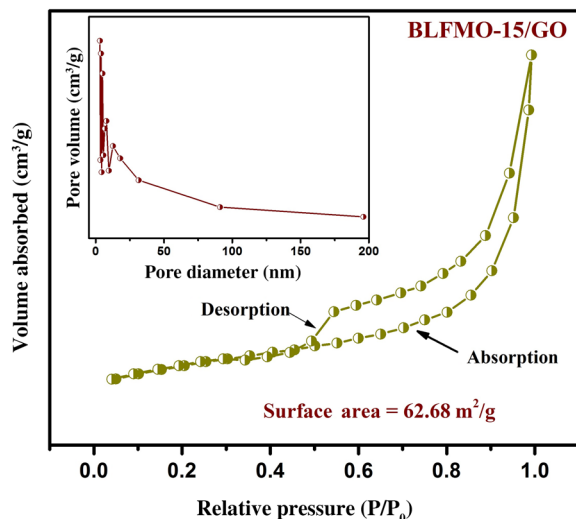


**Figure 5.** Nitrogen adsorption–desorption isotherm with BET specific surface area for the BLFMO-10/GO nanohybrid. Inset: BJH pore size distribution curve.

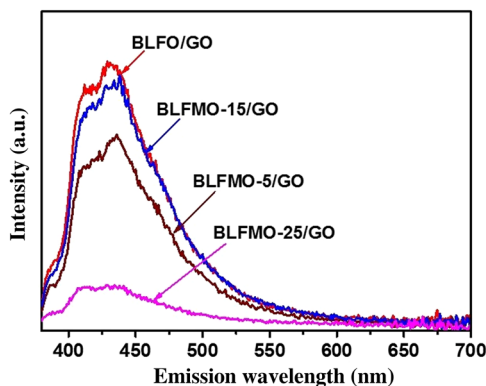


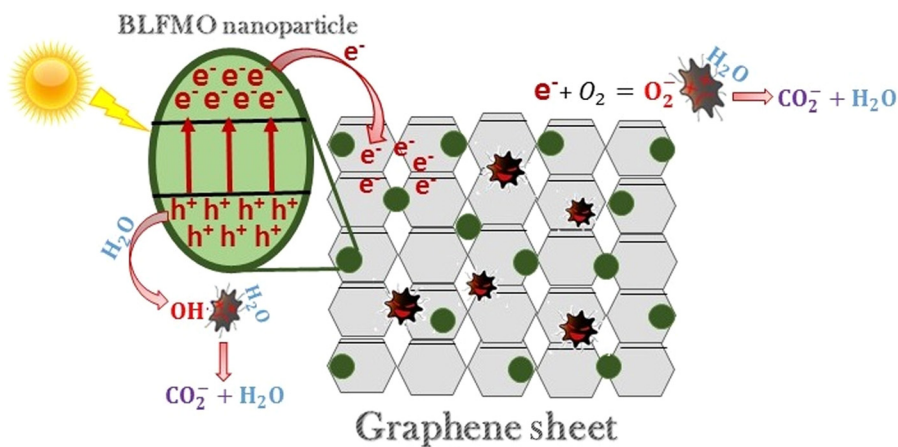
**Figure 6.** PL spectra of BLFMO-5/GO and BLFMO-15/GO nanohybrids.

helps in deterioration of pollutants with the formation of water and carbon dioxide as by-products.

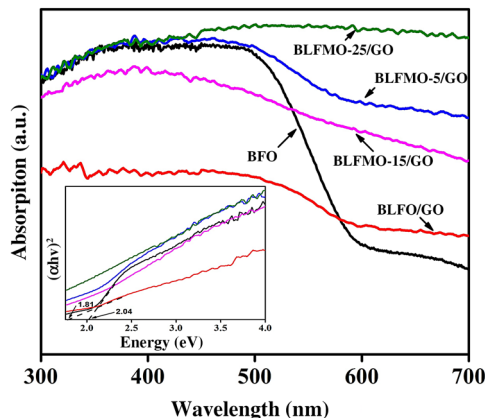
It was found that the optical band-gap of nanohybrids of  $\text{BiFeO}_3$  with GO is significantly tuned to their pure form. The DRS for band-gap evaluation of BLFMO/GO series are presented in Fig. 8.

Two bulging characteristics of the reflectance spectra were noticed. First of all, the BLFMO/GO series exhibit approximately the similar optical absorption conduct as shown by pure  $\text{BiFeO}_3$  nanostructures around the 300–400 nm UV range, but also present a considerably higher visible light absorption in the range of 400–800 nm, near to peak limit of our reflectance measurements. Furthermore, the BLFMO/GO absorption is enough decreased within the range of 300–400 nm and is fairly superimposed with pure  $\text{BiFeO}_3$  and BLFO/GO at 400 nm and above. The sudden decline in absorption above 400 nm has been recorded by other researchers too<sup>[55]</sup> and was assigned to the  $\text{BiFeO}_3$  (pure sample) band edge. These features indicate that the nanohybrid of BLFMO with GO was favorable for visible to IR absorption. The near edge optical absorption is based upon Kubelka–Munk function,  $(\alpha h\nu) = A(h\nu - E_g)^{n/2}$  where  $h$  and  $E_g$  are Planck's constant and band-gap energy while  $\nu$  is the light frequency and  $A$  is a constant.<sup>[56]</sup>

The plots based on  $(\alpha h\nu)^2$  versus  $h\nu$  shown in the inset of Fig. 8 provide the optical band-gaps of pure  $\text{BiFeO}_3$  with BLFMO/GO nanohybrids. By extrapolating the smooth part of these plots toward the  $x$ -axis we can determine the band-gap energies ( $E_g$ ) of the samples. Correspondingly, the band-gap energy for  $\text{BiFeO}_3$  was 2.04 eV which is well comparable with already recorded results.<sup>[28,31,57]</sup> An increment in dopant concentration decreases the band-gap. Hence the measured reduced band-gap energies were found within the range of 2.04–1.81 eV for BLFO/GO. The decrease in the band-gap energy empowers the improvement in photocatalytic behavior of  $\text{BiFeO}_3$ ,<sup>[58]</sup> further reducing the band-gap of



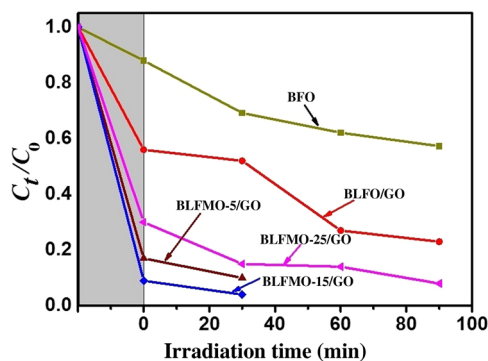
**Figure 7.** Photocatalytic mechanism of BLFMO–graphene nanocomposites.



**Figure 8.** UV-vis absorption spectra for  $\text{BiFeO}_3$ , BLFO, and BLFMO/GO; the inset is the measurement of the bands.

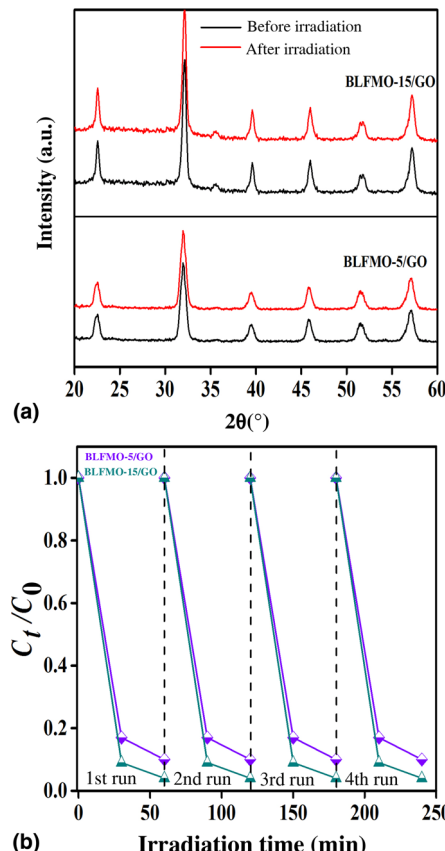
BLFMO-5/GO and BLFMO-15/GO to 1.81 and 1.75 eV, respectively. For the small alterations in optical absorption for BLFMO-25/GO within the visible light range, it was quite difficult to calculate the outbreak of the decrement in optical absorption, as shown in Fig. 8 (inset) which is due to the limited impurity states. The photocatalysis of pure BFO and BLFMO/GO was verified by checking the elimination of organic dye pollutant CR in the presence of visible light.

Figure 9 shows photo-degradation effectiveness of  $\text{BiFeO}_3$  and BLFMO/GO nanohybrids under visible light. Excellent photocatalytic results were obtained for BLFMO-5/GO and BLFMO-15/GO among which CR was significantly degraded within the time interval of 30 min. The CR removal was approximately negligible for the BFO photocatalyst. The overall degradation relies over both catalytic (under dark conditions) and photocatalytic (presence of light radiations) activity of nanohybrids. The catalytic activity is highest in the BLFMO-15/GO nanohybrid (91%) which is attributed to more dye adsorption over the hybrid surface due to having a higher specific surface area while in BLFO/GO,



**Figure 9.** The photocatalytic activities of BLFMO/GO nanohybrids in comparison with pure  $\text{BiFeO}_3$ .

BLFMO-GO, and BLFMO-25/GO it is 44%, 82%, and 70%. As compared with catalytic activity, the photocatalytic activity is higher in BLFMO-25/GO (15%) due to having a low carrier recombination rate (low PL intensity) while the photocatalytic activity in BLFO/GO, BLFMO-5/GO, and BLFMO-15/GO is 4%, 8%, and 5%. The total degradation rate among BLFO/GO, BLFMO-5/GO, BLFMO-15/GO, and BLFMO-25/GO is 77%, 90%, 96%, and 92%. The removal rate of dye was significantly improved by inserting GO inside BLFMO/GO nanohybrids which helps in increasing specific surface area and active transfer of charge carriers toward active sites due to being a trapping site for electrons. The XRD patterns of the BLFMO-5/GO and BLFMO-15/GO nanocomposites before and after photocatalytic reaction are shown in Fig. 10(a). The crystal structure of both, BLFMO-5/GO and BLFMO-15/GO photocatalysts did not change after photocatalytic reaction. There was no presence of any other secondary phase at the end of reaction. Furthermore, the stability of these photocatalysts was also inspected up to four cycles and is illustrated in Fig. 10(b); the photocatalytic efficiency of nanohybrids was not affected with the repetition of the reaction. The constancy in the catalytic activity confirms that BLFMO/GO nanohybrids



**Figure 10.** (a) XRD curves of BLFMO/GO nanohybrids in the beginning and at the end of photocatalytic reaction. (b) Stable photocatalytic curves for the BLFMO-5/GO and BLFMO-15/GO nanohybrids up to four cycles.

are well persistent photocatalysts and show very good potential for different applications.

## Conclusion

BFO co-doped nanoparticles (BLFO and BLFMO) were prepared via the sol-gel fabrication technique and the GO was chemically synthesized. The BLFO/GO and BLFMO/GO nano-hybrids were prepared by a co-ppt method. Well embedded mesoporous nanoparticle-two-dimensional sheet-like nanostructures were obtained and analyzed for photocatalytic application. BLFMO-5/GO and BLFMO-15/GO were obtained with sizeable surface areas of 30.06 and 62.68 m<sup>2</sup>/g, respectively. The enhanced catalytic activity was observed in nanohybrids (96% in 30 min) because of the incorporation of GO layers within the nanoparticles. Graphene, due to the presence of more reactive sites, results in more electron-hole pair generation with a low recombination rate, hence, an increase in the photocatalytic degradation. Higher surface area encourages the nanohybrids to absorb a broad spectrum of visible light thus, encourages the fast degradation of organic dye. The cost effective preparation and higher photocatalytic efficiency of these BLFMO/GO nanohybrids make them suitable candidates for useful commercial applications.

## Acknowledgment

The Higher Education Commission (HEC) of Pakistan funded the research activity under the Project #39/HEC/R&D/PAKUS/2017/783 and 6040/Federal/NRPU/R&D/HEC/2016 to carry out part of the research work within Pakistan. This work was also funded by benevolent support of United States Agency for International Development (USAID) under the Pakistan-U.S. Science & Technology Cooperation Program grant. The essence does not inevitably express the perspectives of the US Government.

## References

- R. Srivastava, and B.C. Yadav: Ferrite materials: introduction, synthesis techniques, and applications as sensors. *Int. J. Green Nanotechnol.* **4**, 141–154 (2012).
- M. Tsuji, Y. Wada, T. Yamamoto, T. Sano, and Y. Tamura: CO<sub>2</sub> decomposition by metallic phase on oxygen-deficient Ni(II)-bearing ferrite. *J. Mater. Sci. Lett.* **15**, 156–157 (1996).
- J. Choung, Z. Xu, and J. Finch: Role of complexing agents in ferrite formation under ambient conditions. *Ind. Eng. Chem. Res.* **38**, 4689–4693 (1999).
- A. Rondinone, A. Samia, and Z. Zhang: A chemometric approach for predicting the size of magnetic spinel ferrite nanoparticles from the synthesis conditions. *J. Phys. Chem. B* **104**, 7919–7922 (2000).
- A. Golman: *Modern Ferrite Technology*, 2nd ed. (Springer Science & Business Media, Pittsburgh, USA, 2006).
- G. Catalan, and J. F. Scott: Physics and applications of bismuth ferrite. *J. Adv. Mater.* **21**, 2463–2485 (2009).
- M. Zaleski: Thermally stimulated processes related to photochromism of scandium doped sillenites. *J. Appl. Phys.* **87**, 4279–4284 (2000).
- P. Borse, U. Joshi, S. Ji, J. Jang, E. Jeong, H. Kim, and J. Lee: Band gap tuning of lead-substituted BaSnO<sub>3</sub> for visible light photocatalysis. *Appl. Phys. Lett.* **90**, 1–3 (2007).
- T. Kimura, T. Goto, H. Shintani, K. Ishizaka, T. Arima, and Y. Tokura: Magnetic control of ferroelectric polarization. *Nature* **426**, 55–58 (2003).
- E. Nippolainen, A. Kamshilin, V. Prokoev, and T. Jaskelainen: Combined formation of a self-pumped phase-conjugate mirror and spatial subharmonics in photorefractive sillenites. *Appl. Phys. Lett.* **78**, 859–861 (2001).
- O. Roussak, and H.A. Gesse: *Applied Chemistry: A Textbook for Engineers and Technologists*, 2nd edn. (Springer Science & Business Media, New York, 2012).
- C. Lee, X. Wei, J. Kysar, and J. Hone: Measurement of the elastic properties and intrinsic strength of monolayer graphene. *Science* **321**, 385–388 (2008).
- L. A. Falkovsky: Optical properties of graphene. *J. Phys.: Conf. Ser.* **129**, 1–7 (2008).
- W. Choi, and J.W. Lee: *Graphene: Synthesis and Applications*, 1st ed. (CRC Press, Boca Raton, USA, 2016).
- R. Mertens: *The Graphene Handbook*, 2016 ed. (lulu.com, USA, 2016).
- A. M. Silva, and S. A. Carabineiro: *Advances in Carbon Nanostructures*. (InTech, USA, 2016).
- R. Asahi, T. Morikawa, T. Ohwaki, K. Aoki, and Y. Taga: Visible-light photocatalysis in nitrogen-doped titanium oxides. *Science* **293**, 269–272 (2001).
- Y. Zhang, Z.R. Tang, X.Z. Fuand, and Y.J. Xu: TiO<sub>2</sub>-graphene nanocomposites for gas-phase photocatalytic degradation of volatile aromatic pollutant: is TiO<sub>2</sub>-Graphene truly different from other TiO<sub>2</sub>-carbon composite materials. *ACS Nano* **4**, 7303–7314 (2010).
- H. Tonga, S.X. Ouyang, Y.P. Bi, N. Umezawa, M. Oshikiri, and J.H. Ye: Nano-photocatalytic materials: possibilities and challenge. *Adv. Mater.* **24**, 577–584 (2012).
- F.K. Meng, Z.L. Hong, J. Arndt, M. Li, M.J. Zhi, F. Yang, and N.Q. Wu: Visible light photocatalytic activity of nitrogen-doped La<sub>2</sub>Ti<sub>2</sub>O<sub>7</sub> nanosheets originating from band gap narrowing. *Nano Res.* **5**, 213–221 (2012).
- M.Y. Zhang, C.L. Shao, J.B. Mu, X.M. Huang, Z.Y. Zhang, Z.C. Guo, P. Zhang, and Y.C. Liu: Hierarchical heterostructures of Bi<sub>2</sub>MoO<sub>6</sub> on carbon nanofibers: controllable solvothermal fabrication and enhanced visible photocatalytic properties. *J. Mater. Chem.* **22**, 577–584 (2012).
- Z.W. Seh, S.H. Liu, M. Low, S.Y. Zhang, Z.L. Liu, A. Mlayah, and M.Y. Han: Janus Au-TiO<sub>2</sub> Photocatalysts with strong localization of plasmonic near fields for efficient visible light hydrogen generation. *Adv. Mater.* **24**, 2310–2314 (2012).
- Y. Zhou, C.L. Muhich, B.T. Neltner, A.W. Weimer, and C.B. Musgrave: Growth of Pt particles on the anatase TiO<sub>2</sub> (101) surface. *J. Phys. Chem. C* **116**, 12114–12123 (2012).
- L.N. Kong, W. Chen, D.K. Ma, Y. Yang, S.S. Liu, and S.M. Huang: Size control of Au@Cu<sub>2</sub>O octahedra for excellent photocatalytic performance. *J. Mater. Chem.* **22**, 719–724 (2012).
- A. Fujishima, and K. Honda: Electrochemical photolysis of water at a semiconductor electrode. *Nature* **238**, 37–38 (1972).
- V. Stengl, D. Popelkova, and P. Vlaci: TiO<sub>2</sub>-graphene nanocomposite as high performance photocatalysts. *J. Phys. Chem. C* **115**, 25209–25218 (2011).
- Y.Y. Liang, H.L. Wang, H.S. Casalongue, Z. Chen, and H.J. Dai: TiO<sub>2</sub> nanocrystals grown on graphene as advanced photocatalytic hybrid materials. *Nano Res.* **3**, 701–705 (2010).
- F. Gao, X. Chen, K. Yin, S. Dong, Z. Ren, F. Yuan, Z.Z.T. Yu, and J. M. Liu: Visible-light photocatalytic properties of weak magnetic BiFeO<sub>3</sub> nanoparticles. *Nature* **238**, 2889–2892 (1972).
- J. An, L. Zhu, N. Wang, Z. Song, Z. Yang, D. Du, and H. Tang: Photo-Fenton like degradation of tetrabromobisphenol A with graphene BiFeO<sub>3</sub> composite as a catalyst. *Chem. Eng. J.* **219**, 225–237 (2013).
- Z. Li, Y. Shen, C. Yang, Y. Lei, Y. Guan, Y. Lin, D. Liu, and C.W. Nan: Significant enhancement in the visible light photocatalytic properties of BiFeO<sub>3</sub>-graphene nanohybrids. *J. Mater. Chem. A* **1**, 823–829 (2013).
- U.A. Joshi, J.S. Jang, P.H. Borse, and J.S. Lee: Microwave synthesis of single-crystalline perovskite BiFeO<sub>3</sub> nanocubes for photoelectrode and photocatalytic applications. *Appl. Phys. Lett.* **92**, 1–3 (2008).
- Q.J. Ruan, and W.D. Zhang: Tunable morphology of Bi<sub>2</sub>Fe<sub>4</sub>O<sub>9</sub> crystals for photocatalytic oxidation. *J. Phys. Chem. C* **113**, 4168–4173 (2009).
- S. Sun, W. Wang, L. Zhang, and M. Shang: Visible light-induced photocatalytic oxidation of phenol and aqueous ammonia in flowerlike Bi<sub>2</sub>Fe<sub>4</sub>O<sub>9</sub> suspensions. *J. Phys. Chem. C* **113**, 12826–12831 (2009).

34. T. Soltani and M. H. Entezari: Photolysis and photocatalysis of methylene blue by ferrite bismuth nanoparticles under sunlight irradiation. *J. Mol. Catal. A: Chem.* **377**, 197–203 (2013).
35. T. Soltani, and M.H. Entezari: Solar photocatalytic degradation of RB5 by ferrite bismuth nanoparticles synthesized via ultrasound. *Ultrason. Sonochem.* **20**, 1245–1253 (2013).
36. N. Zhang, D. Chen, F. Niu, S. Wang, L. Qin, and Y. Huang: Enhanced visible light photocatalytic activity of Gd-doped BiFeO<sub>3</sub> nanoparticles and mechanism insight. *Sci. Rep.* **6**, 1–11 (2016).
37. S. Irfan, S. Rizwan, Y. Shen, R. Tomovska, S. Zulfiqar, M.I. Sarwar, and C.-W. Nan: Mesoporous template-free gyroid-like nanostructures based on La and Mn co-doped Bismuth ferrites with improved photocatalytic activity. *RSC Adv.* **6**, 114183–114189 (2016).
38. S. Irfan, S. Rizwan, Y. Shen, L. Li, A. Asfandiyar, S. Butt, and C.-W. Nan: The gadolinium (Gd<sup>3+</sup>) and tin (Sn<sup>4+</sup>) co-doped BiFeO<sub>3</sub> nanoparticles as new solar light active photocatalysts. *Sci. Rep.* **7**, 1–12 (2017).
39. S. Wang, D. Chen, F. Niu, N. Zhang, L. Qin, and Y. Huang: Pd cocatalyst on Sm-doped BiFeO<sub>3</sub> nanoparticles: synergistic effect of a Pd cocatalyst and samarium doping on photocatalysis. *RSC Adv.* **6**, 34574–34584 (2016).
40. A. Peigney, C. Laurent, E. Flahaut, R.R. Bacsa, and A. Rousset: Specific surface area of carbon nanotubes and bundles of carbon nanotubes. *Carbon. N. Y.* **39**, 507–514 (2001).
41. Q. Xiang, J. Yu, and M. Jaroniec: Graphene-based semiconductor photocatalysts. *Chem. Soc. Rev.* **41**, 782–796 (2012).
42. J.F. Dai, T. Xian, L.J. Di, and H. Yang: Preparation of BiFeO<sub>3</sub>-graphene nanocomposites and their enhanced photocatalytic activities. *J. Nanomater.* **2013**, 1–5 (2013).
43. A. Sun, H. Chen, C. Song, F. Jiang, X. Wang, and Y. Fu: Magnetic Bi<sub>25</sub>FeO<sub>40</sub>-graphene catalyst and its high visible-light photocatalytic performance. *RSC Adv.* **3**, 4332–4340 (2013).
44. H. Sun, Y. Liu, Y. Zhang, L. Lv, J. Zhou, and W. Chen: Synthesis of Bi<sub>2</sub>Fe<sub>4</sub>O<sub>9</sub>/reduced graphene oxide composite by one-step hydrothermal method and its high photocatalytic performance. *J. Mater. Sci.: Mater. Electron.* **25**, 4212–4218 (2014).
45. Z.T. Hu, J. Liu, X. Yan, W.D. Oh, and T.T. Lim: Low-temperature synthesis of graphene/Bi<sub>2</sub>Fe<sub>4</sub>O<sub>9</sub> composite for synergistic adsorption-photocatalytic degradation of hydrophobic pollutant under solar irradiation. *Chem. Eng. J.* **262**, 1022–1032 (2015).
46. T. Soltani, and B.K. Lee: Sono-synthesis of nanocrystallized BiFeO<sub>3</sub>/reduced graphene oxide composites for visible photocatalytic degradation improvement of bisphenol A. *Chem. Eng. J.* **306**, 204–213 (2016).
47. F.G. Garcia, C.S. Riccardi, and A.Z. Simes: Lanthanum doped BiFeO<sub>3</sub> powders: syntheses and characterization. *J. Alloys. Compd.* **501**, 25–29 (2010).
48. G.S. Arya, and N.S. Negi: Effect of In and Mn co-doping on structural, magnetic and dielectric properties of BiFeO<sub>3</sub> nanoparticles. *J. Phys. D: Appl. Phys.* **46**, 1–8 (2013).
49. A. Trapalis, N. Todorova, T. Giannakopoulou, N. Boukos, T. Speliotis, D. Dimotikali, and J. Yu: TiO<sub>2</sub>/graphene composite photocatalysts for NO<sub>x</sub> removal: a comparison of surfactant stabilized graphene and reduced graphene oxide. *Appl. Catal. B: Environ.* **180**, 637–647 (2016).
50. Y. Li, M.S. Cao, D.W. Wang, and J. Yuan: High-efficiency and dynamic stable electromagnetic wave attenuation for La doped bismuth ferrite at elevated temperature and gigahertz frequency. *RSC Adv.* **5**, 77184–77191 (2015).
51. Q. Xu, Y. Sheng, M. Khalid, Y. Cao, Y. Wang, X. Qiu, W. Zhang, M. He, S. Wang, S. Zhou, Q. Li, D. Wu, Y. Zhai, W. Liu, P. Wang, Y.B. Xu, and J. Du: Magnetic interactions in BiFe<sub>0.5</sub>Mn<sub>0.5</sub>O<sub>3</sub> films and BiFeO<sub>3</sub>/BiMnO<sub>3</sub> superlattices. *Sci. Rep.* **5**, 1–8 (2015).
52. W.B. Hu, Y. Liu, R.L. Withers, T.J. Frankcombe, L. Noren, A. Snashall, M. Kitchin, P. Smith, B. Gong, H. Chen, J. Schiemer, F. Brink, and J. Wong-Leung: Electron-pinned defect-dipoles for high-performance colossal permittivity materials. *Nat. Mater.* **12**, 821–826 (2013).
53. L. Shi, L. Liang, J. Ma, F. Wang, and J. Sun: Remarkably enhanced photocatalytic activity of ordered mesoporous carbon/g-C<sub>3</sub>N<sub>4</sub> composite photocatalysts under visible light. *Dalton Trans.* **43**, 7236–7244 (2014).
54. G. Liao, S. Chen, X. Quan, H. Yu, and H. Zhao: Graphene oxide modified g-C<sub>3</sub>N<sub>4</sub> hybrid with enhanced photocatalytic capability under visible light irradiation. *J. Mater. Chem.* **22**, 2721–2726 (2012).
55. N. Miriyala, K. Prashanthi, and T. Thundat: Oxygen vacancy dominant strong visible photoluminescence from BiFeO<sub>3</sub> nanotubes. *Phys. Status Solidi RRL* **7**, 668–671 (2013).
56. P. Kubelka, and F. Munk: Ein Beitrag zur optik der farbanstriche. *Tech. Phys.* **12**, 593–601 (1931).
57. R. Guo, L. Fang, W. Dong, F. Zheng, and M. Shen: Enhanced photocatalytic activity and ferromagnetism in Gd doped BiFeO<sub>3</sub> nanoparticles. *J. Mater. Chem. C* **114**, 21390–21396 (2010).
58. N.S.A. Satar, A.W. Aziz, M.K. Yaacob, M.Z.A. Yahya, O.H. Hassan, T.I. T. Kudin, and N.H.M. Kaus: Experimental and first-principles investigations of lattice strain effect on electronic and optical properties of biotemplated BiFeO<sub>3</sub> nanoparticles. *J. Phys. Chem. C* **120**, 26012–26020 (2016).